Inorganic Chemistry

Article

pubs.acs.org/IC

Acid–Base Chemistry in the Formation of Mackay-Type Icosahedral Clusters: μ_3-Acidity Analysis of Sc-Rich Phases of the Sc–Ir System

Yiming Guo, Timothy E. Stacey,[†] and Daniel C. Fredrickson*

Department of Chemistry, University of Wisconsin–Madison, 1101 University Avenue, Madison, Wisconsin 53706, United States

Supporting Information

ABSTRACT: The crystal structures of intermetallic phases offer a wealth of geometrical features (helices, multishelled clusters, and host–guest motifs) whose formation has yet to be explained or predicted by chemical theory. A recently developed extension of the acid–base concept to metallic systems, the μ_3-acidity model, provides an avenue for developing this understanding for intermetallics formed from transition metals. In this Article, we illustrate how this approach can be used to understand one of the most striking geometrical entities to emerge in intermetallic chemistry, the Mackay cluster of icosahedral quasicrystals. We present μ_3-acidity analyses, based on DFT-calibrated Hückel calculations, for a series of Sc–Ir intermetallics: ScIr (CsCl-type), Sc_2Ir (Ti_2Ni-type), $Sc_{11}Ir_4$, and the Mackay cluster containing phases $Sc_{57}Ir_{13}$ and $Sc_{44}Ir_7$. We begin by illustrating that a μ_3-acidity model correctly predicts that each of these phases is stable relative to disproportionation into their neighboring compounds when a common set of Hückel parameters and d-orbital occupancies is used. Next, we explain these results by developing a relationship between the distance distribution of homoatomic contacts within an atom's coordination sphere and the μ_3-neutralization it experiences. For a given average homoatomic distance, the role of heteroatomic contacts is higher when the distribution of homoatomic contacts is narrower. This effect is key to the strength of the acid–base neutralization of the Sc-rich phases, where the Sc atoms find a scarcity of Ir atoms from which to obtain neutralization. Under these circumstances, Sc–Ir contacts should be maximized, whereas the number and distance variations of the Sc–Sc contacts should be minimized. These expectations are borne out by the observed crystal structures. In particular, the Mackay clusters of $Sc_{57}Ir_{13}$ and $Sc_{44}Ir_7$, in which a central Ir atom is icosahedrally coordinated by a pentagonal dodecahedral array of face-sharing Sc octahedra, represent a natural way of merging the competing needs for enhancing Sc–Ir interactions while diminishing those between the Sc atoms.

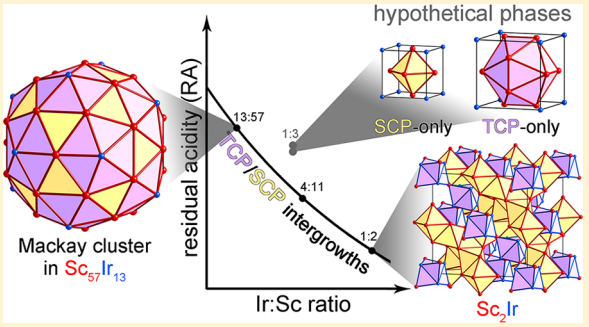

1. INTRODUCTION

As a group, chemists are not often accustomed to embracing bulk metals and alloys as the products of chemical reactions. Yet, at the level of their crystal structures, intermetallic phases exhibit a vast structural diversity, expressing familiar chemical factors such as electron count, atomic sizes, and electronegativity, although in a language that hitherto remains mostly unclear.[1−3] One fulfilling way of conceptually approaching these compounds is to take a traditional chemical concept, such as the octet rule, and explore the limits of its applicability in the metallic state. For example, the evolving adaptation of the octet and Wade–Mingos rules to intermetallics has led to the productive fields of Zintl phases[4−6] and polar intermetallics[7] as well as to a sharpening of the distinction between localized and metallic bonding.[8,9] In this Article, we will consider another chemical notion whose domain of applicability to metals is still being explored: that of acids and bases.

Compared to the ionic and covalent bonding principles embodied in the Zintl model, the acidity concept has a shorter history in metals. In the 1970s, Brewer and Wengert interpreted the high thermodynamic stability of intermetallics formed between early and late transition metals in terms of "generalized Lewis-acid–base interactions."[10] Here, electron pairs on late transition metal atoms were envisioned as being donated to empty d-orbitals on the early transition metal atoms. More recently, we used the method of moments, as applied to DFT-calibrated Hückel calculations, to derive a definition of acidity in terms of the filling of the electronic density of states curves of metals: μ_3-acidity.[11] In this model, transition metal atoms are grouped into acids and bases based on the difference between their d-orbital occupations and an ideal value determined by the third moment (μ_3) of their model DOS curves. The potential for these acidic and basic elements to neutralize each other was found to explain the formation of a wide range of intermetallics,[11] the stability ranges of the common CsCl- and Laves phase-type structures,[11,12] and the presence of intriguing structural features such as helical tubes of Ti in $Ti_{21}Mn_{25}$.[13]

This progress opens new questions about the potential for acid/base ideas to elucidate intermetallic structures, including (1) how many of the intriguing geometrical motifs encountered

Received: March 4, 2014
Published: May 6, 2014

   dx.doi.org/10.1021/ic500510s | Inorg. Chem. 2014, 53, 5280–5293

in intermetallic phases can be understood from this point of view and (2) if acid/base matching is important to phase stability, then why do intermetallic phase diagrams frequently exhibit compounds at several compositions rather than a single phase at a ratio that optimizes this matching?

An excellent model system for pursuing answers to these questions is offered by the Sc−Ir binary phase diagram. Elemental Sc and Ir represent strong μ_3-acids and bases, respectively, and the potential here for acid−base interactions to influence structural chemistry is thus particularly high. The system also exhibits a wide range of structures (Figure 1).[14,15]

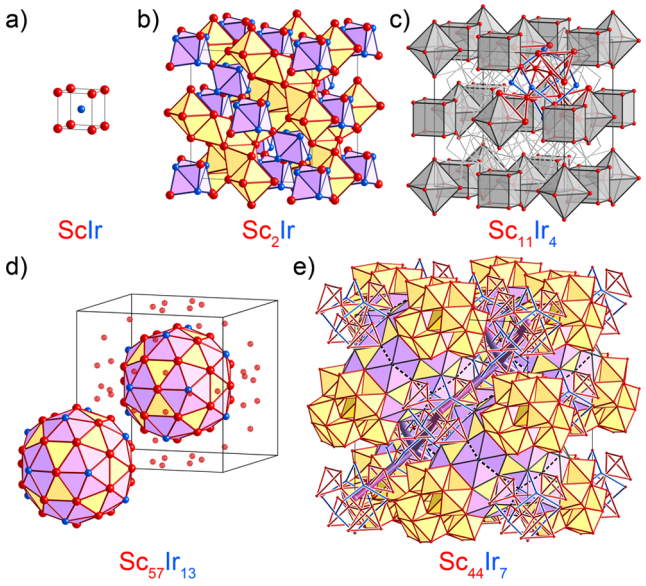

Figure 1. Structural diversity in the Sc−Ir system. Crystal structures are shown for the Sc-rich side of the system: (a) ScIr, (b) Sc_2Ir, (c) $Sc_{11}Ir_4$, (d) $Sc_{57}Ir_{13}$, and (e) $Sc_{44}Ir_7$.

The variety on just the Sc-rich side of the diagram ranges from the simple CsCl-type ScIr,[14,15] to a derivative of the γ-brass structure in $Sc_{11}Ir_4$,[16] and onward to the complex structures based on Mackay clusters[17] (a prominent unit in Mackay-type quasicrystals[18]) in $Sc_{57}Ir_{13}$[19] and $Sc_{44}Ir_7$.[20]

Using the μ_3-acidity model, we will see that the progression of structures illustrated in Figure 1 provides a means of achieving optimal neutralization for varying ratios of Sc and Ir. In fact, each of the complex structures in the figure is predicted by the model to be stable to disproportionation into its neighbors in the phase diagram. Determining how the structures accomplish this stability will take us toward a deeper understanding of the differences of interatomic interactions in two limiting forms of atomic packing, simple close-packed (scp) and tetrahedral close-packed (tcp) arrangements, and how these packing modes can play complementary roles in neutralization. The beautiful Mackay clusters of $Sc_{57}Ir_{13}$ and $Sc_{44}Ir_7$ will feature prominently as examples of outcomes of the collaboration between scp and tcp motifs. In this way, the μ_3-acidity approach will offer an explanation for the local arrangements in Mackay-type quasicrystals and their approximants, whose long-range features are usually interpreted in reciprocal space through the Mott−Jones model.[21]

2. TECHNICAL PROCEDURES

Crystallographic Information Files (CIFs) for the structures studied in this Article were obtained from the Inorganic Crystal Structure Database (ICSD).[22−24] Full structural optimization and subsequent band structure/density of states (DOS) calculations were carried out with the Vienna Ab Initio Simulation Package (VASP),[25,26] using the generalized gradient approximation (GGA) of Perdew and Wang (PW91) and the projected augmented wave (PAW) potentials[27,28] provided with the program. Further technical details on the VASP calculations, including k-point meshes and energy cutoffs, are listed in the Supporting Information.

The band structure and DOS results were then used for the parametrization of a simple Hückel model. This fitting process was accomplished using our program eHtuner.[12] eHtuner calls the program YAeHMOP[29] for performing simple Hückel calculations as a subroutine. Sc and Ir parameters were refined for each of the phases depicted in Figure 1. These results were then averaged across the phases to obtain a common set of Sc and Ir parameters to facilitate comparisons between the structures. The Hamiltonian matrix elements obtained using these DFT-calibrated Hückel parameters then served as the basis of our analyses using the method of moments and the μ_3-acidity model described below. Tables of the DFT-calibrated Hückel parameters used in this work are provided in the Supporting Information.

3. μ_3-ACIDITY APPLIED TO THE Sc−Ir SYSTEM

As we described previously, a strong foundation for adapting the acid/base concept to metals is provided by the method of moments.[11−13] In this method, the moments of the electronic density of states (DOS) distributions, $\mu_n = \int_{-\infty}^{\infty} E^n \mathrm{DOS}(E)\, dE$, serve as bridges between the geometrical details of a crystal structure and the electronic structure that it underlies.[30−33] The lower order moments (n = 0, 1, and 2) are familiar from the statistical analysis of distributions: μ_0 is simply the total area of a DOS curve, μ_1/μ_0 is the mean energy of the distribution, and μ_2 provides the variance of the distribution. Because μ_2 measures the degree of dispersion in a band structure, it is often associated with the magnitudes of the interatomic interactions.[32,34] The higher-order moments contain information about other aspects of the DOS curve's shape, and in order to focus on them, it is common to scale and translate the DOS curve such that the early moments achieve the standard values of $\mu_0 = 1$, $\mu_1 = 0$, and $\mu_2 = 1$.

The next moment, μ_3, has properties that are of particular relevance to the notion of acidity, as is illustrated in Figure 2. Here, standardized DOS plots with $\mu_3 < 0$, $\mu_3 = 0$, and $\mu_3 > 0$ are compared. All three curves show bimodal distributions but with different relative sizes of the high- and low-energy peaks. For $\mu_3 = 0$, the two peaks are of equal size, symmetrically distributed around $E = 0$. For $\mu_3 > 0$, the mean energy remains as $E = 0$,

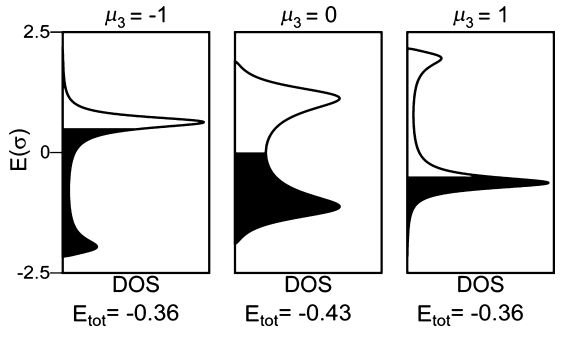

Figure 2. Role of the third moment, μ_3, in optimizing the shape of a density of states (DOS) distribution for a specific electron count. The shaded portion of the DOS curves corresponds to the occupation of half of the available electronic states.

dx.doi.org/10.1021/ic500510s | Inorg. Chem. 2014, 53, 5280−5293

but this is now achieved through balancing a small peak at very high energies with a large peak at an only moderately low energy. The $\mu_3 < 0$ curve represents the reverse case, in which a small peak at very low energies is balanced by a large peak at an only moderately high energy. μ_3 thus controls the relative number of states above or below the mean energy (and the DOS minimum separating the peaks).

In this way, μ_3 is closely tied to what electron count would be most favorable for a DOS curve. For instance, in the case of a half-filled system, $\mu_3 = 0$ provides a distribution in which the lower peak will be completely filled (unlike the $\mu_3 > 0$ case) and none of the upper peak is occupied (in contrast to the $\mu_3 < 0$ case). In fact, as we demonstrated previously,[11] for simple DOS curves defined by just μ_0–μ_4 (with μ_0–μ_2 standardized as described above), the lowest energy is achieved for a given band filling when the μ_3 value places a DOS minimum at the Fermi energy (the depth of which is determined by μ_4). From this, an analytical relationship can be derived between the percent filling of a DOS distribution and the optimal μ_3 value. Inverting this relationship yields a prediction of the ideal electron count for a system as a function of its μ_3 value, i.e., what electron count is expected to fill the DOS curve to a DOS minimum as in the curves of Figure 2.

In providing this prediction of a μ_3-ideal electron count, μ_3 makes a connection to the acidity concept. Systems that have electron counts in excess of the μ_3-ideal would be expected to be eager to donate electrons in an analogous manner to Lewis bases. Meanwhile, systems whose electron counts fall short of their μ_3 ideal value would benefit from receiving electrons as do Lewis acids. This electron excess or deficiency is quantified by the system's μ_3-acidity = the μ_3-ideal electron count − the actual electron count.

In our hands, the μ_3-acidity approach has been particularly helpful in understanding the structures formed between first-row transition metals, where the predictions of the μ_3-acidity model are expected to be particularly relevant: d-orbital-only models of the transition metals yield DOS curves that show roughly bimodal character similar to that seen in Figure 2.

The μ_3-acidities of the elemental transition metals are listed in Table 1, in which we have expanded upon our earlier work to include the 4d and 5d metals. All of the transition metals share an ideal d-orbital band filling of about 45% (whether the structure is the bcc, fcc, or α-Mn type). This common μ_3 ideal leads to a progression in the acidities (see color coding in Table 1), with early transition metals appearing as strongly acidic, the late transition metals appearing as strongly basic, and a neutral point occurring at the Cr column. These trends mirror well the original generalized Lewis acid–base picture of Brewer and Wengert[10] and the tendency for intermetallic phases to form between late and early transition metals.

Table 1. μ_3-Acidities of the Transition Metals (Electrons/Atom)

Sc	Ti	V	Cr	Mn	Fe	Co	Ni	Cu
3.04	2.11	0.52	-0.09	-1.22	-2.27	-3.12	-3.89	-4.80
Y	Zr	Nb	Mo	Tc	Ru	Rh	Pd	Ag
2.52	2.02	0.92	-0.17	-0.94	-1.66	-3.11	-4.06	-4.86
Lu	Hf	Ta	W	Re	Os	Ir	Pt	Au
2.69	2.40	1.29	0.15	-0.44	-1.68	-2.64	-3.71	-4.60

With the μ_3-acidity model, we can also examine how well combining these elements into particular crystal structures provides neutralization of these acid–base properties. This is illustrated in Figure 3, in which the model DOS curves of

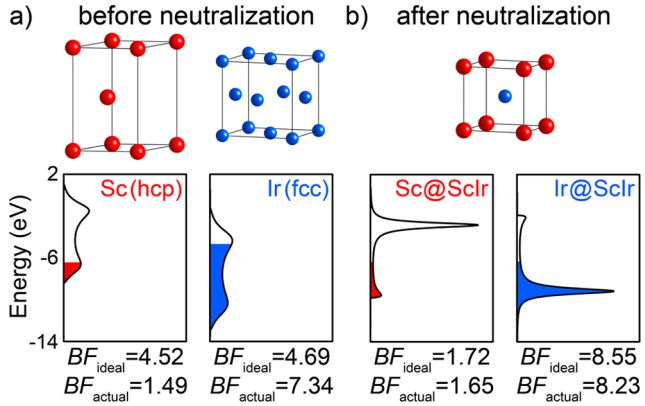

Figure 3. Projected DOS curves of (a) elemental Sc and Ir and (b) the CsCl-type ScIr binary phase. Before the formation of ScIr, Sc is relatively electron-deficient (analogous to Lewis acids) and Ir is electron-rich (analogous to Lewis bases). Formation of the intermetallic compound reshapes the DOS curves for the two elements so that their distributions are better tailored to their occupation by electrons. BF: band filling in electrons per atom.

elemental Sc (strong acid) and Ir (moderately strong base) are compared with their projected DOS (pDOS) distributions in the CsCl-type intermetallic ScIr. For both of the elemental phases, the DOS distributions exhibit bimodal shapes with the upper and lower peaks being of nearly equal size, but the Sc and Ir curves are under- and overoccupied, respectively, relative to the propitious minima near the middles of the curves, as expected from their acid/base characters.

Upon combining the Sc and Ir to form ScIr, the shapes of the DOS curves change dramatically (Figure 3b). For Sc, the majority of the distribution is shifted to higher energies, leaving a small number of states at low energies. The Ir is affected in the opposite sense, with most of the DOS distribution now lying at low energies. These new shapes appear to be much better-tailored to the electron counts of the two elements. The remaining Sc states at the lower peak are just sufficient to accommodate its small band filling, whereas the large peak for Ir is well-suited in its high band filling. In fact, both curves are filled to a common pseudogap at ca. −6 eV. The strong acid and base character of the two elements have well-neutralized each other in the formation of the binary phase.

The DOS for elemental Sc is also centered at a higher energy than that of elemental Ir, reflecting the lower electronegativity of Sc. When we consider that the Sc states are interacting with the Ir states from above, the shapes of the neutralized DOS curves of ScIr have a straightforward interpretation. The lower- and higher-energy peaks in the two curves represent the bonding and antibonding portions of the DOS distributions. Because the Ir orbitals are lower in energy, they contribute more to the bonding states. Thus, their DOS is weighted toward the lower-energy peak. Conversely, the higher-energy Sc orbitals contribute more to the antibonding states, and their DOS distribution is skewed toward the upper peak. The shift in the third moments for the Sc and Ir DOS curves can then be largely traced to the difference in electronegativity between the two elements. Indeed, the ability of a μ_3-acid and μ_3-base to

dx.doi.org/10.1021/ic500510s | Inorg. Chem. 2014, 53, 5280–5293

neutralize each other is strongly dependent on a correlation between μ_3-acidity and electronegativity: moving from right to left in Table 1 corresponds to both increasing μ_3-acidity and decreasing electronegativity.

In our earlier paper focusing on $Ti_{21}Mn_{25}$,[13] we derived an analytical relationship for this effect, showing that the change in μ_3 for the DOS of a transition metal resulting from heteroatomic interactions with a different transition metal element is given by

$$\Delta\mu_3 \approx \frac{\mu_2^{A-B}}{\mu_2} \cdot \frac{\Delta H_{ii}}{\sigma} \quad (1)$$

Here, μ_2^{A-B} and μ_2 are the strengths of heteroatomic (in our case, between Sc and Ir) and total (homoatomic + heteroatomic) interactions, respectively. ΔH_{ii} corresponds to the difference in ionization energies (IEs) between the d-orbitals of the two elements (IE of heteroatom − IE of central atom), and σ is the standard deviation of the atom's DOS curve relative to the mean E. The change in μ_3 is then proportional to two factors: (1) the fraction of interaction strength that arises from heteroatomic interactions and (2) the energy difference between the d-orbitals of the two transition metal elements relative to the total dispersion of the d-orbitals along the E axis. Of these, the former varies much more from one structure to the next, and as such, the change in μ_3 upon introducing heteroatomic interactions is largely a function of the relative strengths of homo- and heteroatomic interactions.

From the close agreement between the band filling and DOS minima in ScIr, it would seem that the balance between heteroatomic and homoatomic interactions is nearly optimal for its Sc and Ir atoms. This agreement is quantified by the residual acidity (RA) of each atom (i.e., the μ_3-acidity that remains on that atom after the formation of the binary intermetallic). In Figure 4, the RAs for ScIr are compared to the μ_3-acidities of the elemental phases (elemental acidities) of the component elements. Here, the neutralization is seen to be substantial: Ir goes from being basic by 2.64 electrons to being slightly acidic by only 0.32 electrons. Likewise, Sc's acidity is reduced from 3.04 electrons/atom in the elemental phase to 0.07 in ScIr.

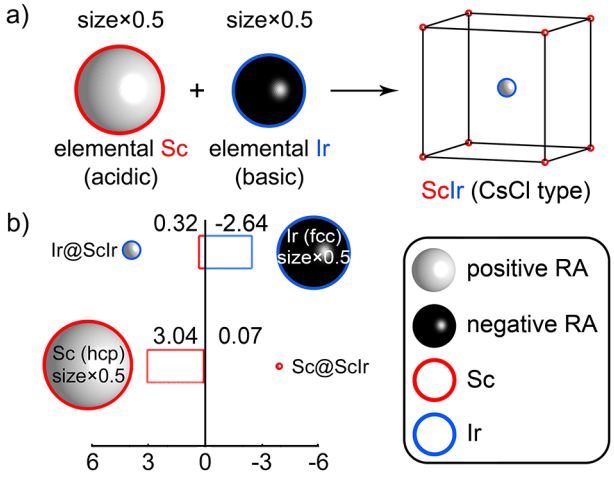

Figure 4. μ_3 analysis of ScIr. (a) Formation of ScIr from elemental Sc and Ir. (b) Bar graph of residual acidity of Sc and Ir before and after formation of ScIr. Color scheme: white spheres and black spheres indicate positive and negative RA, respectively, whereas their radii show the magnitudes of their RAs. Red and blue outlines of the spheres represent Sc and Ir atoms, respectively.

Figure 4 also introduces a graphical representation that will be useful when we discuss more complex structures. The white and black spheres represent positive and negative μ_3-acidity, respectively, with their radii showing the acidity magnitudes. In this plotting scheme, the strength of the neutralization occurring upon the formation of ScIr is apparent in the drastic reduction in the sizes of the RA spheres.

Given that the neutralization is nearly ideal in the CsCl-type phase ScIr, one might wonder how neutralization will be achieved in compounds with other compositions. To explore this question, we carried out μ_3-acidity analyses on all of the Sc-rich phases in the Sc−Ir phase diagram. To prevent distortions of the results from differences in the qualities of our DFT-calibrated Hückel models for the compounds, we used a common set of Sc and Ir parameters. We also used a constant value for the Ir and Sc d-orbital occupations, noting that the d-orbital occupations in our Hückel models change very little from structure to structure.[11,13]

The average Sc RAs are plotted in Figure 5 as a function of the Ir/Sc ratio, and the Supporting Information contains a similar curve for the average RAs taken over all atoms. As could be anticipated from the higher acidity of Sc than that of Ir, the average RA of the compounds increases as the fraction of Sc is increased from ScIr to elemental Sc. However, the progression of RA points varies substantially from the linear curve that would result from a simple interpolation between the ScIr and Sc points. Instead, the series bends downward to follow a convex curve.

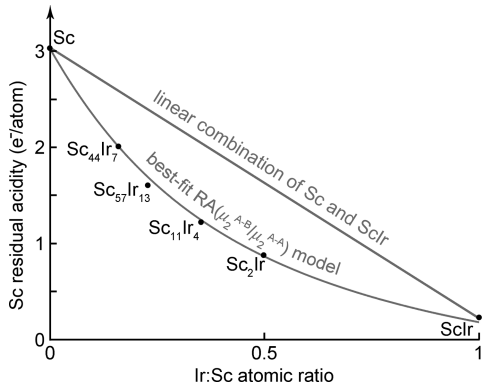

Figure 5. Plot of net Sc residual μ_3-acidity (RA) per atom as a function of composition for the phases of the Sc-rich side of the Sc−Ir phase diagram. The convex form of the curve indicates that each phase has a lower residual acidity than a linear combination of its neighbors of the same overall composition. For details concerning the best-fit RA model curve, see the Supporting Information.

The convex shape of this curve has important ramifications for the relative degrees of μ_3 neutralization of each of the structures. The RA point for any of the Sc-rich phases lies below any linear combination of other phases in the plot with the same net composition. In other words, the μ_3-acidity model predicts that each of the Sc-rich phases plotted in Figure 5 is stable to decomposition into neighboring phases, in agreement with experimental observations. In this way, every one of these compounds is predicted to offer advantages in terms of μ_3 neutralization for their particular Sc/Ir ratio. Over the course of this Article, we will see how the complex structures lying along the curve of Figure 5 achieve this feat.

dx.doi.org/10.1021/ic500510s | Inorg. Chem. 2014, 53, 5280−5293

4. TETRAHEDRAL AND SIMPLE CLOSE PACKINGS AND THE MOMENTS

One clue to the structural origins of the μ_3 neutralization in the Sc−Ir phases is the types of atomic packing they contain. As we will soon show in more detail, the most complex Sc−Ir phases combine motifs from two basic categories of packing patterns encountered in intermetallic phases: simple close-packed (scp) and tetrahedrally close-packed (tcp) arrangements. scp refers to simple periodic sphere packings that achieve high packing densities, such as face-centered close packing (fcc), hexagonal close packing (hcp), and double-hexagonal close packing (dhcp). These represent the densest possible packings of an infinite array of equally sized spheres.[35] The regularity of these structures is also apparent in the shapes of its interstitial spaces, which are generally ideal (or nearly so) octahedra and tetrahedra.

tcp compounds, such as Cr_3Si-type and $MgCu_2$-type phases, are based on a different structural principle. Rather than arraying themselves into a pattern conducive to periodicity, the atoms assemble into tetrahedral clusters so that all of the interstitial spaces in the structure are distorted tetrahedra. The differences in the types of interstices found in tcp and scp structures also result in different coordination polyhedra around the atoms, as is shown in Figure 6. Whereas in the scp structures, only two coordination environments are encountered, the 12-coordinate cuboctahedron and twinned cuboctahedron, tcp phases can contain a larger variety polyhedra (known as Frank−Kasper polyhedra), with a range of coordination numbers.[36,37]

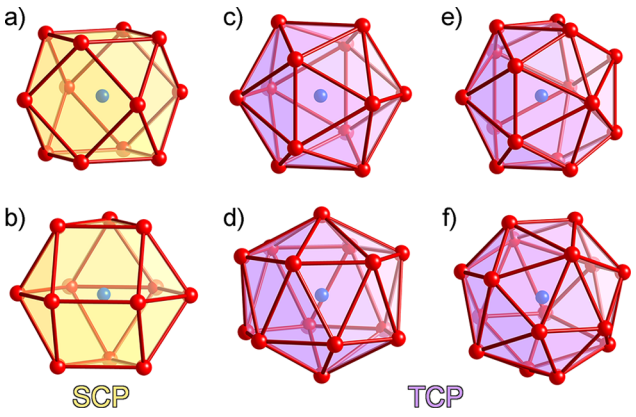

Figure 6. Comparison of the coordination polyhedra prevalent in simple and tetrahedrally close-packed (scp and tcp) structures. (a, b) Cuboctahedron and twinned-cuboctahedron of the scp fcc and hcp structures, respectively. (c−f) Examples of the Frank−Kasper polyhedra appearing in tcp structures.

This dichotomy of intermetallic crystal structures into tcp and scp accounts for many (although certainly not all) simple intermetallic phases. In the most complex Sc−Ir phases shown in Figure 1, however, the nearly ideal octahedra (yellow) expected for scp structures appear alongside with clusters of tetrahedra (purple) familiar from tcp arrangements. The Sc−Ir phases thus represent more complicated structures containing both scp units and tcp-type fragments, which we will refer to in this Article as tcp/scp intergrowth phases.

How might this incorporation of both tcp and scp features in the Sc−Ir phases facilitate their μ_3 neutralization? The first step in answering this question is to see how the structural differences between tcp and scp arrangements are reflected in the moments, μ_n's, of their DOS curves. For the DFT-calibrated simple Hückel calculations that we are using for our μ_3-acidity analyses, there is a direct relationship between the μ_n values and the features of a crystal structure, as are encoded in the Hamiltonian matrix elements (H_{ij}'s) between pairs of atomic orbitals (AOs). Each μ_n value is simply the sum of the products of H_{ij}'s corresponding to n-step closed paths through the crystal structure[31]

$$\mu_n = \sum_{i_1}^{\text{all AOs}} \sum_{i_2}^{\text{all AOs}} \cdots \sum_{i_n}^{\text{all AOs}} H_{i_1 i_2} H_{i_2 i_3} \cdots H_{i_{n-1} i_n} H_{i_n i_1} \tag{2}$$

In this way, the μ_n values can be directly calculated from the local features of a crystal structure.

As we see in eq 1, the relative magnitudes of the total μ_2 value for an atom of interest (AOI) and its component that arises from heteroatomic contacts ($\mu_2^{\text{A−B}}$) is of particular importance to μ_3 neutralization. For these quantities, eq 2 reduces to

$$\mu_2 = \sum_{i_1}^{i_1 \in \text{AOI}} \sum_{i_2}^{\text{all AOs}} H_{i_1 i_2} H_{i_2 i_1} = \sum_{i_1}^{i_1 \in \text{AOI}} \sum_{i_2}^{\text{all AOs}} |H_{i_1 i_2}|^2 \tag{3}$$

and

$$\mu_2^{\text{A−B}} = \sum_{i_1}^{i_1 \in \text{AOI}} \sum_{i_2}^{i_2 \in \text{element B}} |H_{i_1 i_2}|^2 \tag{4}$$

In both of these sums, the principal components are the squares of the Hamiltonian matrix integrals between the atomic orbitals on interacting atoms. For any pair of atoms, this summation is a simple function of the distance separating the two atoms (Figure 7). At small distances, this sum is at a maximum because of the high overlap between the AOs on the two atoms. As the distance is increased, the function decreases essentially exponentially as the overlap is diminished.

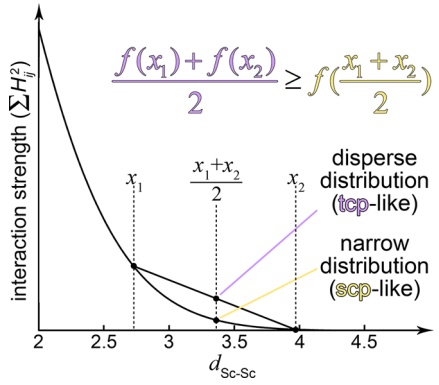

Figure 7. Comparison of average interatomic interaction strength (as measured by the μ_2 contribution from a pair of atoms) between packings with relatively narrow (scp-like) and wide (tcp-like) distributions of interatomic distances. A more disperse distribution on $d_{\text{Sc−Sc}}$ results in a higher average interaction strength. The dispersity of the wider $d_{\text{Sc−Sc}}$ distribution is exaggerated relative to that observed in tcp structures to make the effect more visible.

The relative sizes of μ_2 and $\mu_2^{\text{A−B}}$ for the atoms of a structure are then going to be largely determined by the number of significant interatomic contacts and the distances associated with these contacts. Here, we arrive at an important difference

dx.doi.org/10.1021/ic500510s | Inorg. Chem. 2014, 53, 5280−5293

between tcp and scp structures: they have very different distributions to their interatomic distances. This is illustrated in Figure 8 by comparing histograms of the interatomic distance

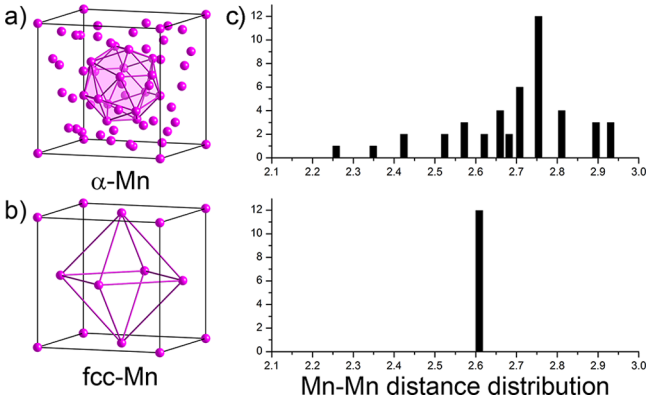

Figure 8. Histograms of the interatomic distances in the (a) α- and (b) γ-(fcc) allotropes of elemental Mn. This example serves to contrast the interatomic distance distributions of (a) tcp and (b) scp structures.

distributions of two allotropes of manganese, α-Mn[38] (tcp) and γ-Mn[39] (fcc, scp). Whereas the scp γ-Mn has a single near-neighbor distance of 2.6 Å, the tcp α-Mn distribution exhibits a much broader distribution of Mn−Mn distances ranging from ca. 2.25 to 2.95 Å.

This result can be explained by the different ways in which scp and tcp structures fill space. In the scp arrangement of the fcc structure, space is filled easily by a combination of ideal octahedra and tetrahedra, which share faces. The ideality of these polyhedra means that only a single edge length is needed. The situation is much more complicated for tcp structures in that ideal tetrahedra alone cannot fill 3D space. Distortions of the tetrahedra, which broaden the interatomic distance distribution, are therefore essential in a tcp phase.

Although the average interatomic distance remains similar on moving from the scp γ-Mn to the tcp α-Mn, the different widths of the distributions has a profound effect on the μ_2 values calculated for the atoms of these structures. The dependence of μ_2 interaction strength on interatomic distance appears in Figure 7 as a convex function. Because of this shape, the average of two μ_2 values at different distances will be higher than the μ_2 value at the average distance, an effect known in mathematics as Jensen's inequality. More generally, the greater the dispersion of a distance distribution for any given average distance, the greater will be the expected average μ_2 interaction strength.

From this analysis, we can see that tcp motifs will generally confer higher average μ_2 interatomic interaction strengths than scp features. As we will begin to explore in the next section, these properties can be used by a structure to adjust the balance of homoatomic and heteroatomic interactions in the search for optimal μ_3 neutralization.

5. Sc_2Ir: HOW SCP/TCP INTERGROWTH ENHANCES μ_3 NEUTRALIZATION

Now that we have seen generally how the different packing types present in the Sc−Ir phases may influence interatomic interaction strengths, let us return to the ScIr phase we discussed in Section 3 and how its neutralization is affected by introducing more Sc into the system. In the formation of ScIr (Figure 4), the Sc atoms go from being strongly acidic in the elemental phase to nearly neutralized, whereas the Ir atoms change from strongly basic to weakly acidic. At a 1:1 stoichiometry, Sc and Ir are thus well-matched in acid/base strength.

As we move on to the next phase in the system, Sc_2Ir, the fraction of Sc in the structure increases and the balance of acid/base strengths is shifted. There are now twice as many Sc atoms as Ir atoms, which would suggest that the over-neutralization observed for Ir in ScIr should be drastically increased. Meanwhile, Sc will have fewer interactions with Ir atoms, so underneutralization of Sc is likely. Yet, the RA results of Figure 5 (in agreement with experiment) predict that the reaction ScIr + Sc → Sc_2Ir should be favorable.

More detailed results of the μ_3-acidity analysis of Sc_2Ir confirm the favorability of its formation (Figure 9). The RA of

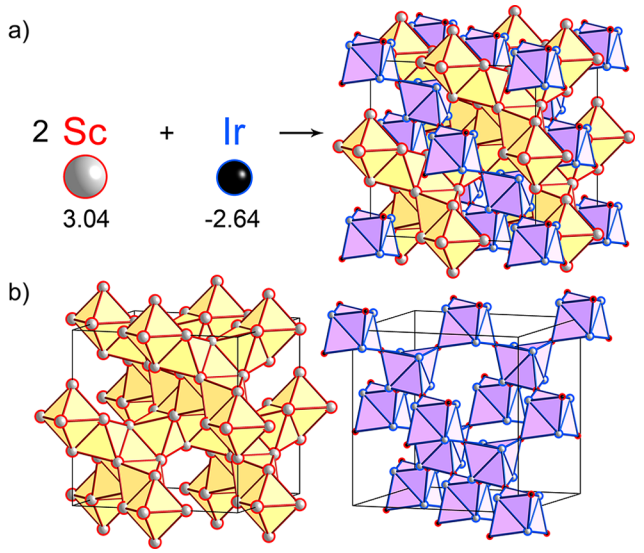

Figure 9. μ_3 neutralization in the formation of Sc_2Ir. (a) Comparison of the acidities calculated for Sc and Ir in their elemental phases and in the Sc_2Ir phase. (b) Separate plots of the residual acidities (RAs) in the two interpenetrating diamond networks of the structure: the scp framework composed of Sc octahedra and the tcp framework composed of Sc and Ir stella quadrangula. The yellow and purple colors are assigned to illustrate scp and tcp packings, respectively, in this Article. See the caption to Figure 4 for RA plotting conventions.

Sc atoms drop from 3.04 electrons/atom (elemental Sc) to 0.69 (Sc1) and −0.24 (Sc2), and Ir atoms are also neutralized from −2.46 to 0.40. This represents surprisingly strong neutralization given the expectations mentioned earlier. Although the neutralization for any given Sc or Ir is not as high as would be found in ScIr, this is more than offset by the opportunity to provide neutralization to not one but two Sc atoms per formula unit.

How has the phase managed to maintain strong neutralization with a Sc/Ir ratio so far away from the nearly ideal 1:1 composition? The answer lies in the beautiful crystal structure of Sc_2Ir. This phase adopts the Ti_2Ni structure type (*cF*96), which can be visualized as two interpenetrating diamond networks (Figure 9): one is composed solely of face-sharing Sc octahedra (yellow), whereas the other is built from vertex-sharing Sc/Ir stella quadrangula (purple). The first of these frameworks is built from octahedra and tetrahedra (not shown) and locally resemble scp arrangements. The stella quadrangula framework consists entirely of tetrahedra, as does its immediate

dx.doi.org/10.1021/ic500510s | *Inorg. Chem.* 2014, 53, 5280−5293

surroundings. In this way, the network forms the backbone of a tcp domain in the structure. Altogether, the Sc_2Ir structure can be then seen as a double-diamond structure in which scp and tcp domains interpenetrate each other.

This tcp/scp intergrowth character has consequences for the level of μ_3 neutralization in the phase. Recall that the shift in the μ_3 value for an atom upon going from an elemental to binary structure follows the equation

$$\Delta\mu_3 \approx \frac{\mu_2^{A-B}}{\mu_2} \cdot \frac{\Delta H_{ii}}{\sigma}$$

When an element experiences a threat of underneutralization, as do the Sc atoms in Sc_2Ir, its atoms need to maximize their heteroatomic interactions (μ_2^{A-B}) while minimizing internal interactions (μ_2^{A-A}) to make the overall μ_2 as small as possible. For an element threatened with overneutralization (Ir in Sc_2Ir), its atoms need to maximize homoatomic interaction to increase the denominator in the above equation.

The use of scp and tcp arrangements offers a means of adjusting these important μ_2^{A-B} and μ_2^{A-A} values. Because scp packing has a more uniform interatomic distance distribution and hence a weaker overall μ_2 interaction value than tcp, arranging the homoatomic or heteratomic networks into scp patterns minimizes the corresponding μ_2^{A-A} or μ_2^{A-B} values. tcp patterns, in contrast, can be used to maximize these quantities.

For Sc_2Ir, the Sc atoms are faced with a paucity of Ir neighbors. They thus arrange themselves into an scp arrangement (minimizing μ_2^{Sc-Sc}) that wraps around the Ir atoms to create icosahedra (tcp, maximizing μ_2^{Sc-Ir}). The Ir atoms, in contrast, are challenged by an overabundance of Sc neighbors. For them, scp Sc−Ir arrangements would be preferable to tcp for reducing their μ_2^{Ir-Sc} terms, but as a minority element, they have little say here. They can, however, dictate the geometry for the Ir−Ir interactions: they assemble into tcp patterns to maximize their μ_2^{Ir-Ir} value.

The observed crystal structure of Sc_2Ir provides an excellent demonstration of these effects. The majority element, scandium, packs in an octahedral pattern (the scp diamond framework of octahedra), thus minimizing Sc−Sc interaction, whereas the minority atom, iridium, has tcp environments (participating in the tcp framework of stella quadrangula). The Ir atoms have icosahedral coordination, a typical coordination polyhedron in tcp structures, which facilitates interaction both with the Sc (to maximize the Sc's neutralization by Ir) and other Ir atoms (to minimize the overneutralization of Ir by Sc). The combination of these effects makes the formation of Ti_2Ni-type Sc_2Ir favorable from Sc and ScIr.

From this analysis of Sc_2Ir, a general principle can be distilled that will recur in the more complex Sc−Ir phases: when considering structures formed in an intermetallic system based on a strong μ_3-acid and a strong μ_3-base, scp packing is preferred within the majority element framework, whereas tcp packing is favored between the two component elements.

6. μ_3-ACIDITY ANALYSIS OF $Sc_{11}Ir_4$

Upon moving from Sc_2Ir toward more Sc-rich phases, the first compound we encounter is $Sc_{11}Ir_4$.[16] The experimental data so far on this phase is somewhat inconclusive, as its original description notes that it may actually be a suboxide, containing interstitial oxygen atoms. Elemental analysis indicated the presence of oxygen, but all attempts failed in refining the position of the oxygen atoms from the Fourier electron density maps. As we saw in Figure 2, the μ_3-acidity model predicts the stability of this compound even without the consideration of possible oxygen incorporation. It is useful, then, to examine how its structural features are conducive to μ_3 neutralization.

The reported $Sc_{11}Ir_4$ structure can be seen as a 2 × 2 × 2 supercell of a primitive cubic array of γ-brass clusters (Figure 10), in which each pair of adjacent γ-brass clusters are mirror

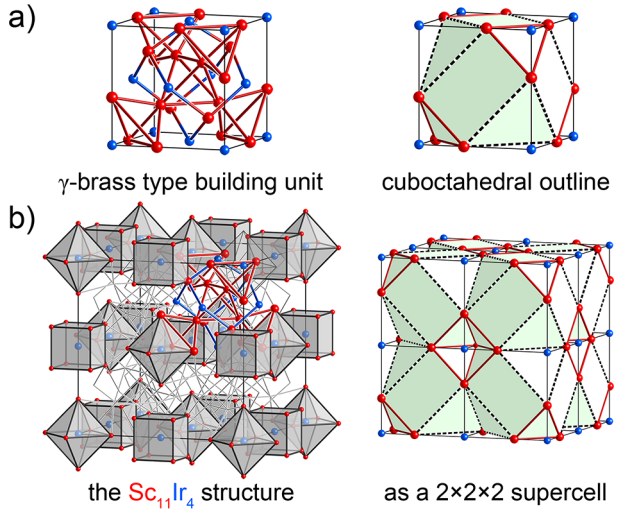

Figure 10. The crystal structure of $Sc_{11}Ir_4$. (a) γ-Brass-type building block of $Sc_{11}Ir_4$ and a schematic representation of it. The structure of $Sc_{11}Ir_4$ as a 2 × 2 × 2 supercell of the building block in panel a.

images of each other across planes of shared atoms parallel to the {100} planes. Additional Ir atoms fit into the cubic and octahedral void spaces (gray polyhedra in Figure 10b, left) that arise between the γ-brass clusters.

Because the γ-brass structure is an example of tcp arrangements, its prominence in $Sc_{11}Ir_4$ would suggest that this structure is rich in tcp character. As per our tcp/scp intergrowth principle described above, tcp domains would be expected to maximize the Sc−Ir interactions, as would be crucial for neutralizing the majority Sc atoms given that the Sc/Ir ratio is close to 3:1. To optimize these interactions fully, we might expect the Sc−Sc interactions to trace out scp fragments to achieve homogeneous interatomic distances.

Hints of scp-like features are evident in Sc_8 cubes and Sc_6 octahedra occurring between the γ-brass fragments, which could provide a means of narrowing the Sc−Sc distance distribution. These two types of polyhedra are arranged in a NaCl-type pattern across the unit cell, with the corners of the octahedra pointing toward the faces of the cubes to make square antiprisms at the interfaces.

However, although the presence of such cubes and octahedra of Sc is suggestive of scp character, the distance distribution within the Sc sublattice is, in fact, quite sizable (2.93 to 3.63 Å vs 3.10 to 3.20 Å in the Sc_2Ir structure described in the last section). As such, the Sc sublattice is not expected to be adapted to maximizing the neutralization of the Sc by Sc−Ir contacts. Instead, strong Sc−Ir interactions are pursued through low Sc coordination numbers around the Ir atoms (Ir@Sc_6 octahedra and Ir@Sc_8 cubes), with shorter Sc−Ir distances; the shortest Sc−Ir distance here is 2.59 Å, compared to 2.66 Å for Sc_2Ir.

dx.doi.org/10.1021/ic500510s | Inorg. Chem. 2014, 53, 5280−5293

In Figure 11, we show the μ_3-acidities that result from placing Sc and Ir into the structure of $Sc_{11}Ir_4$. Most Sc atoms have

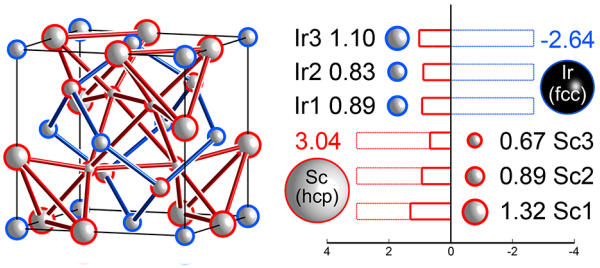

Figure 11. μ_3 analysis of $Sc_{11}Ir_4$. The bar graph shows the neutralization of all symmetry-inequivalent Sc sites and Ir sites.

managed to achieve a reasonable degree of neutralization. However, the Ir atoms suffer from substantial overneutralization compared to that of the Sc–Ir phases discussed earlier. This is a reflection of the absence of Ir–Ir interactions to counteract the effect of the Sc–Ir interactions. Apparently, at this stoichiometry, the Sc atoms have a sufficient majority to outweigh the preferences of the Ir atoms. As we consider more Sc-rich phases, the Ir will continue to be coordinated exclusively by Sc. Also, the use of low coordination numbers around Ir to minimize Sc–Ir distances will quickly become impractical as more Sc atoms need to be accommodated, making the scp arrangements in the Sc sublattice a more essential tool for modulating Sc–Ir interactions.

7. ROLE OF MACKAY CLUSTERS IN μ_3 NEUTRALIZATION IN $Sc_{57}Ir_{13}$

As we add Sc to $Sc_{11}Ir_4$, the first new compound we encounter is $Sc_{57}Ir_{13}$, in which the Sc/Ir ratio is now more than 4:1. Considering that Sc was already underneutralized with $Sc_{11}Ir_4$'s ca. 3:1 ratio, the issue of providing neutralization to the Sc atoms can be seen as becoming increasingly desperate. It is under these dire circumstances that one of the most intriguing structural motifs offered by the Sc–Ir system emerges: the Mackay cluster,[17] a common structural building block in quasicrystals and quasicrystal approximants.[18] The crystal structure of $Sc_{57}Ir_{13}$ ($Sc_{57}Rh_{13}$ structure type, *cP*140) is based on a bcc-type packing of Mackay clusters (Figure 12), with a few interstitial Sc atoms filling in the gaps (whose placement reduces the lattice symmetry from *cI* to *cP*).[19]

A closer examination of the Mackay cluster's structure offers clues to its origins in this Sc-rich system (Figure 13). Traditionally, the Mackay cluster is presented in terms of concentric polyhedral shells (Figures 13a–c).[18] From this viewpoint, the clusters of $Sc_{57}Ir_{13}$ are nucleated by a central Ir-centered Sc icosahedron (Figure 13a), which is enclosed in a Sc icosidodecahedron (Figure 13b), which in turn is decorated by a larger icosahedron of Ir atoms that cap the pentagonal faces of the icosidodecahedron (Figure 13c). This scheme nicely captures the multishelled nature of the Mackay cluster and its icosahedral symmetry.

In considering the potential of this structure for facilitating μ_3 neutralization, it is helpful to seek a description in terms of tcp/scp features (Figure 13d–f). We first note that the triangular faces of the core icosahedron and the shell icosidodecahedron align so that the pairs of triangles face each other in a staggered configuration. The result is that each pair of triangles combines to form an octahedron (Figure 13d), creating a total of 20 Sc

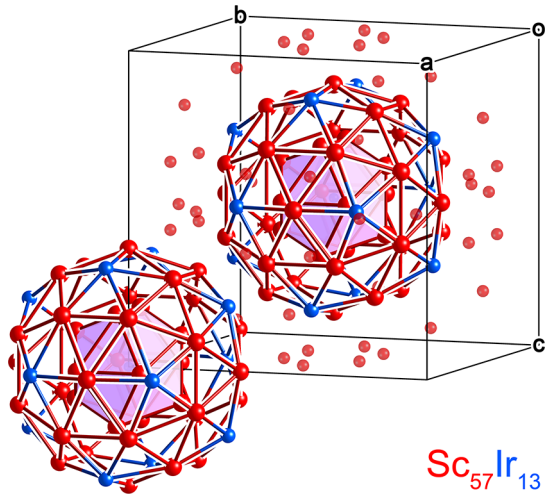

Figure 12. The unit cell of $Sc_{57}Ir_{13}$. The structure can be seen as a bcc packing of isolated Mackay clusters, with additional Sc atoms filling the gaps in between. Note that instead of forming tetrahedral clusters as in Sc_2Ir, all Ir atoms now become isolated from each other in response to the Sc atoms' high demand for Sc–Ir contacts.

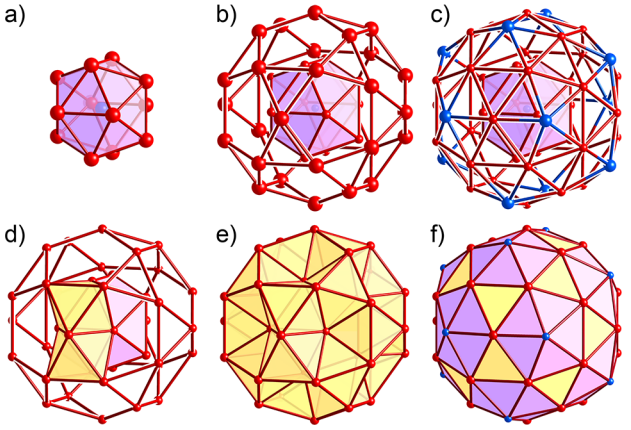

Figure 13. The structure of the Mackay clusters in $Sc_{57}Ir_{13}$. (a–c) Traditional view in terms of concentric shells: (a) Ir-centered icosahedral core, (b) Sc icosidodecahedron shell, and (c) additional Ir atoms finishing the cluster. (d–f) View in terms of tcp/scp intergrowth: (d) the triangles of the core icosahedron (tcp) and of the icosidodecahedron align to produce Sc octahedra, (e) these Sc octahedra share faces to trace out a pentagonal dodecahedron of octahedra (scp), and (f) Ir atoms cap the pentagonal hollows to generate pentagons of face-sharing tetrahedra (tcp).

octahedra around the icosahedron core. These octahedra share faces with each other to form a pentagonal dodecahedron that entirely surrounds the central icosahedron (Figure 13e). The hollows of this dodecahedron of octahedra then serve as spaces for the placement of Ir atoms to create clusters of tetrahedra similar to the Ir-centered icosahedron at the cluster's core (Figure 13f).

This combination of features is expected to be very efficient for achieving μ_3 neutralization. The Sc–Ir interactions are based on tetrahedral packing, where the ability of Ir to neutralize Sc is maximized. In particular, the placement of Ir inside of an icosahedron allows for breaking of the near equivalence of the Sc–Sc and Sc–Ir distances in an scp structure so that the Sc–Ir distances can be shortened without simultaneously decreasing the Sc–Sc distances. Meanwhile, the

dx.doi.org/10.1021/ic500510s | *Inorg. Chem.* 2014, 53, 5280–5293

Sc−Sc interactions are arrayed along the octahedra of scp arrangements, where the low dispersion of distances is expected to minimize their interference with Sc−Ir neutralization.

These predictions are confirmed by a μ_3-acidity analysis of the Mackay cluster of $Sc_{57}Ir_{13}$ (Figure 14). Even though Ir now

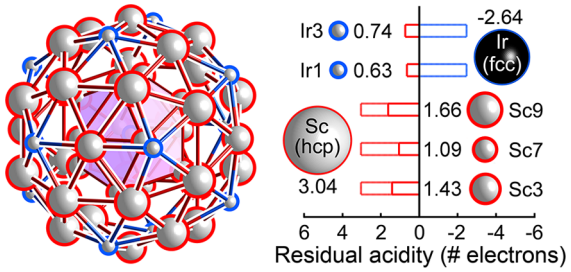

Figure 14. μ_3 neutralization in the Mackay clusters of $Sc_{57}Ir_{13}$. For plotting conventions, refer to the caption of Figure 4.

constitutes less than 20% of the atoms of the phase, the Sc atoms are neutralized to around half of their elemental acidity. Ir, however, is only moderately more overneutralized than in Sc_2Ir despite the Sc/Ir ratio having more than doubled.

In this structure, the role of the Mackay cluster thus emerges as a means for arranging Sc atoms into an scp framework while creating tcp domains to host the Ir atoms. The exceptional degree of neutralization that results may be one electronic reason for the restriction of Mackay clusters in transition metal-based systems to strong μ_3-acid/base combinations. For example, the $Sc_{57}Ir_{13}$ structure is also adopted by Fe,[40] Ru,[19] Rh,[19] and Pt[19] analogues. Likewise, the $Mg_{44}Ir_7$-type structure of $Sc_{44}Ir_7$ to be described in the next section also forms for $Sc_{44}Os_7$.[20] Finally, a Mackay-type quasicrystal and its 1:1 approximant have been reported in the Ti−Zr−Fe system.[41,42]

8. MACKAY$_4$ CLUSTER IN $Sc_{44}Ir_7$

In the previous section, we saw how the $Sc_{57}Ir_{13}$ structure performs extreme structural feats in order to maximize the use of the scarce Ir atoms for neutralizing the Sc atoms. This theme continues in $Sc_{44}Ir_7$, where the Sc/Ir ratio now jumps from 4.4:1 to 6.3:1, with truly magnificent results (Figure 15). $Sc_{44}Ir_7$ adopts the $Mg_{44}Ir_7$ structure type[43] (*cF*408) with a 20.2 Å cubic unit cell having a variety of structural motifs.[20] The complexity of this structure offers multiple ways of interpreting it, such as in terms of γ-brass-type units,[44] the projection of 4D polytopes onto three dimensions,[45] and arrangements of nanoclusters.[46]

The full structure of this compound is analyzed in Figure 15 in terms of tcp and scp features. Because it is based on a fcc lattice, a simple approach to breaking the structure down is to consider the structural units occurring at the high symmetry positions, such as (0, 0, 0), ($^1/_4$, $^1/_4$, $^1/_4$), and ($^1/_2$, $^1/_2$, $^1/_2$), each of which combines with the transitional symmetry to

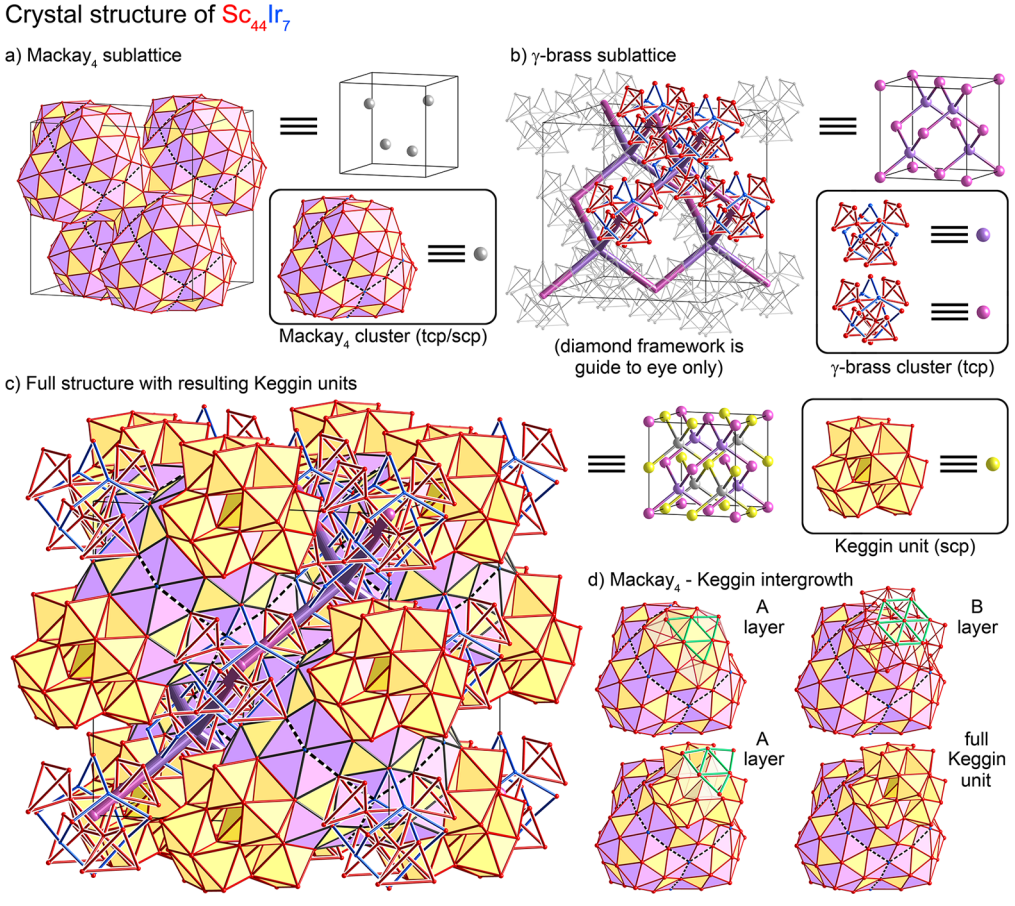

Figure 15. The $Sc_{44}Ir_7$ crystal structure. (a) An fcc packing of Mackay$_4$ units (see Figure 16) centered at the ($^1/_4$, $^1/_4$, $^1/_4$) Wyckoff position, with shared atoms at their boundaries. (b) A diamond network of γ-brass clusters centered at the (0, 0, 0) and ($^3/_4$, $^3/_4$, $^3/_4$) positions. (c) The full crystal structure emerging from the interpenetration of these frameworks, with (d) scp-type Keggin units centered at the ($^1/_2$, $^1/_2$, $^1/_2$) position growing out of corners of the Mackay$_4$ units.

dx.doi.org/10.1021/ic500510s | *Inorg. Chem.* 2014, 53, 5280−5293

create a fcc substructure. At the ($^1/_4$, $^1/_4$, $^1/_4$) position, a Mackay cluster-based unit (Figure 15a) occurs, in which a tetrahedron of Mackay clusters fuse through shared octahedra (see Figure 16 for a more detailed view). We will refer to these tetrahedral units as Mackay$_4$ clusters.

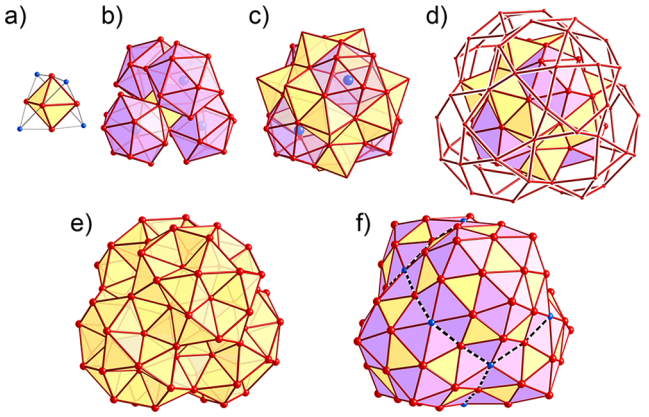

Figure 16. The structure of the Mackay$_4$ cluster. (a) The central octahedron and its tetrahedron of neighboring Ir atoms. (b) Sc icosahedra around the Ir atoms in panel a. (c) Shared octahedra between the Ir@Sc$_{12}$ icosahedra. (d) Outer icosidodecahedral shells surrounding the icosahedra. (e) scp Sc octahedra enclosing the core tcp icosahedra. (f) Completed view of the cluster built from four Mackay clusters linked through shared octahedra.

The gaps between these clusters are filled by two symmetry-distinct tcp-type γ-brass fragments centered at the (0, 0, 0) and ($^3/_4$, $^3/_4$, $^3/_4$) positions (Figure 15b), which together trace out a diamond-type framework. These γ-brass fragments share atoms with the Mackay$_4$ clusters (Figure 15c) so that most Sc atoms in the unit cell partake in both a Sc–Sc scp network and a Sc–Ir tcp network.

Finally, another structural feature emerges at the ($^1/_2$, $^1/_2$, $^1/_2$) position as neighboring Mackay$_4$ clusters join at their corners (Figures 15c,d), forming a Sc-only fragment that resembles the Keggin unit commonly observed in heteropoly acid anions, such as $PMo_{12}O_{40}^{3-}$.[47] Figure 15d shows how the Keggin unit emerges from the layering of close-packed planes of Sc atoms onto the corner of a Mackay$_4$ cluster in the ABAB pattern of the hcp structure. An equivalent series of layers can be drawn along each of the 3-fold axes of the ($^1/_2$, $^1/_2$, $^1/_2$) position's site symmetry so that the Keggin unit can be viewed as arising from the twinning of hcp domains around an fcc core (in a manner analogous to the growth of nanoscale tetrapods from the nucleation of hexagonal wurtzite domains by a cubic sphalerite core[48]). Because the Keggin unit is based on a stacking of close-packed layers, it can be viewed as an scp unit in the structure.

Altogether, the Sc$_{44}$Ir$_7$ unit cell can thus be visualized as an intergrowth of tcp and scp features. The γ-brass clusters and Keggin units represent nearly pure tcp and scp domains, respectively, whereas the Mackay$_4$ units, with their tcp/scp intergrowth character, serve as an interface between these domains.

How does this complex structure facilitate μ_3 neutralization under the Ir-poor circumstances in which this structure finds itself? Let us first consider the Mackay$_4$ cluster. A Mackay$_4$ unit is composed of four interpenetrating Mackay clusters arranged in a tetrahedral manner (Figure 16) so that the core Ir atom of one Mackay cluster becomes a capping Ir atom for the others. Although four isolated Mackay clusters require a total of 13 × 4 = 52 Ir atoms, one Mackay$_4$ cluster demands only 14 Ir atoms if the unshared Ir positions on the outer shell are also replaced by Sc atoms. The fusion of the Mackay$_4$ units could thus be considered as an Ir-conservation measure. The replacement of the unshared, low-priority Ir-type sites with Sc marks the boundary of the scp-Sc Keggin unit, where the homogeneity of the Sc–Sc distances is anticipated to enhance the neutralizing effect of all available Sc–Ir contacts.

The efficacy of this structural arrangement is evident in the calculated μ_3-acidities of Sc$_{44}$Ir$_7$ (Figure 17). Here, we group

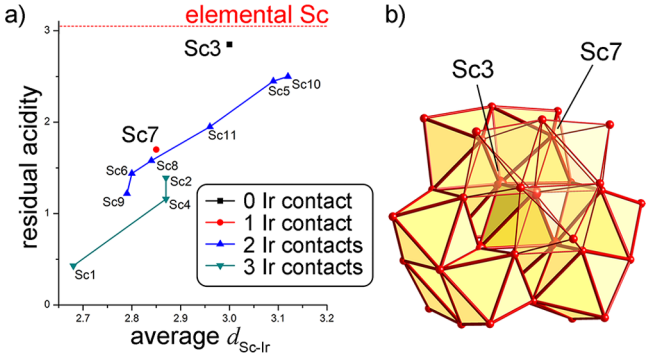

Figure 17. μ_3 analysis of Sc$_{44}$Ir$_7$ (Sc only). (a) Plot of residual acidity against average d_{Sc-Ir}. Fewer and longer Ir contacts result in higher RA. (b) A closer look at the structural context of the Sc3 and Sc7 sites. Sc3 has high residual acidity because it has no Ir contact, but it enhances μ_3 neutralization of Sc7 by scaffolding a scp Sc framework (the Keggin unit).

the residual acidities in a somewhat different way from earlier, dividing the Sc atoms according to their number of Ir neighbors and plotting them according to their average Sc–Ir distance. Most of the Sc sites (aside from Sc3, as we will discuss below) have achieved a reasonable degree of neutralization relative to elemental Sc (horizontal line). Within a given series, the RA acidity increases in a roughly linear fashion with increasing average Sc–Ir distance (and thus lower Sc–Ir interaction strength). Curiously, however, the 1-, 2-, and 3-Ir contact values are not very well separated. In particular, the Sc7 site with only one Sc–Ir contact is nearly as well neutralized as the Sc8 site with two Sc–Ir contacts at a similar distance or the Sc2 site with three Sc–Ir contacts at that distance. Apparently, the structural features around the Sc7 site allow for the very efficient use of its single Sc–Ir contact.

It is with this observation in hand that we can understand the role of the least-well-neutralized Sc site in the structure, Sc3. This site is located at the center of the Keggin units (vertices of the darker yellow tetrahedron at the center in Figure 17b), where it has no access to Ir atoms. Instead, the purpose of the Sc3 atoms appears to be to scaffold the scp Sc framework of the Keggin unit. The unusually well-neutralized Sc7 site occurs in the next shell of Sc atoms surrounding the Sc3 core of the Keggin unit, where it benefits from the scp network built by the Sc3 atoms.

At this point, we have now qualitatively interpreted the high μ_3 neutralization calculated for all of the Sc-rich Sc–Ir phases in terms of the intergrowth of tcp and scp motifs. In the next section, we will derive a more quantitative model for the stability of these phases, in which the RAs of these compounds

dx.doi.org/10.1021/ic500510s | Inorg. Chem. 2014, 53, 5280–5293

can be reduced to a small number of parameters, such as the ratio of Sc and Ir neighbors in the coordination environments, and the width of the distribution of Sc−Sc distances.

9. STABILITY OF SCP/TCP INTERGROWTHS

In our survey of the Sc-rich phases of the Sc−Ir binary system above, a qualitative correlation was obtained between effective μ_3 neutralization and the intergrowth of tcp/scp features. Our arguments throughout this discussion were based on such simple parameters as the relative numbers of Sc and Ir atoms in a given coordination environment and the widths of the distributions of interatomic distances. In this section, we will explore to what degree the stability trends across this system can be reproduced quantitatively using such chemical parameters. As will be revealed, a seemingly simplistic model connecting μ_3-ideal electron counts to the Sc/Ir ratio and the mean and standard deviation of the Sc−Sc distance distribution is surprisingly successful in predicting the stability of these phases.

As we develop our model of the bonding in these phases, we will consider the five observed Sc-Ir phases with a Sc content of ≥50% (ScIr, Sc_2Ir, $Sc_{11}Ir_4$, $Sc_{57}Ir_{13}$, and $Sc_{44}Ir_7$) as well as four more hypothetical phases of either scp-only or tcp-only packing patterns (Table 2) for comparison with the tcp/scp intergrowth phases.

Table 2. Hypothetical Sc−Ir Phases To Be Compared Using the μ_3-Acidity Analysis with Those Experimentally Observed

chemical formula	prototype structure	Pearson symbol	packing type
Sc_3Ir	$AuCu_3$	*cP*4	scp
Sc_3Ir	BiF_3	*cF*16	scp
Sc_3Ir	Cr_3Si	*cP*8	tcp
$Sc_{11}Ir_2$	$Zn_{11}Ir_2$ (γ-brass)	*cI*52	tcp

As a starting point, we recall our earlier equation connecting the change in the μ_3 value of the d-orbitals of an atom upon engaging in heteroatomic interactions

$$\Delta\mu_3 \approx \frac{\mu_2^{\text{A-B}}}{\mu_2}\cdot\frac{\Delta H_{ii}}{\sigma}$$

which shows that the shift in μ_3 will be proportional to the fraction of the variance of the DOS distribution ($\mu_2 = \sigma^2$) that arises from heteroatomic interactions.

With some small rearrangements, this equation can be expressed in terms of the ratio of heteroatomic (A−B) and homoatomic (A−A) contacts in the coordination sphere of the central atom. First, we write the μ_2 factor in the denominator as a sum of the A−B and A−A contributions to it

$$\Delta\mu_3 \approx \frac{\mu_2^{\text{A-B}}}{\mu_2}\cdot\frac{\Delta H_{ii}}{\sigma} = \frac{\mu_2^{\text{A-B}}}{\mu_2^{\text{A-A}}+\mu_2^{\text{A-B}}}\cdot\frac{\Delta H_{ii}}{\sigma} \quad (5)$$

Next, we write the A−A and A−B components of the μ_2 as the product of the number of A and B neighbors of the central atom, n_A and n_B, and the average μ_2 contribution from each neighbor type

$$\Delta\mu_3 \approx \frac{\mu_2^{\text{A-B}}}{\mu_2^{\text{A-A}}+\mu_2^{\text{A-B}}}\cdot\frac{\Delta H_{ii}}{\sigma} = \frac{n_B\overline{\mu_2^{\text{A-B}}}}{n_A\overline{\mu_2^{\text{A-A}}}+n_B\overline{\mu_2^{\text{A-B}}}}\cdot\frac{\Delta H_{ii}}{\sigma} \quad (6)$$

Finally, we divide the numerator and denominator by $n_A\overline{\mu_2^{\text{A-B}}}$ to obtain

$$\Delta\mu_3 \approx \frac{\frac{n_B}{n_A}}{\frac{\overline{\mu_2^{\text{A-A}}}}{\overline{\mu_2^{\text{A-B}}}}+\frac{n_B}{n_A}}\cdot\frac{\Delta H_{ii}}{\sigma} \quad (7)$$

Here, the shift in μ_3 appears as a simple function of (1) the ratio of heteroatomic and homoatomic neighbors for the central atom, n_B/n_A, (2) the ratio of the average interaction strengths for those neighbor types, and (3) the $\Delta H_{ii}/\sigma$ value.

If we consider the $\Delta H_{ii}/\sigma$ value to be essentially constant for any given pair of elements, the effectiveness of a coordination environment in providing μ_3 neutralization then reduces to two parameters, the n_B/n_A and $\overline{\mu_2^{\text{A-A}}}/\overline{\mu_2^{\text{A-B}}}$ ratios, which are closely connected to the structural features that we followed in the previous sections of this Article. The former is tightly correlated with the composition of a compound, which we varied systematically as we moved from ScIr toward more Sc-rich phases. Meanwhile, the latter is a function of the interatomic distance distributions, which differ greatly for the tcp and scp arrangements found in the crystal structures.

In Figure 18, we use eq 7 to plot the predicted ideal band filling (BF) for a Sc atom as a continuous function of $y = n_A/n_B$

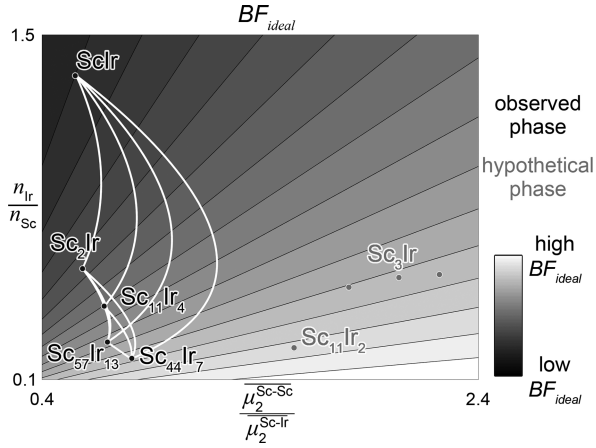

Figure 18. Observed and hypothetical phases overlaid with a contour plot of ideal band filling as a function of the average Sc/Ir ratio in the coordination environments of the Sc atoms as well as relative sizes of the homoatomic and heteroatomic components to the μ_2 (lighter shade corresponds to higher BF_{ideal}). The white curves connecting the observed phases represent calculated stability ranges that assume neutralization of Sc is the dominant driving force for phase formation.

and $x = \overline{\mu_2^{\text{A-A}}}/\overline{\mu_2^{\text{A-B}}}$. The function is presented as on a gray-scale color map in which dark regions correspond to scenarios with the lowest ideal BF and light regions have the highest ideal BF. Because Sc is a strongly acidic element with a relatively low actual BF, the darkest points on the plot essentially represent the most effective neutralization.

As might be expected from our earlier discussion, the best neutralization is found in the upper left corner where the Ir/Sc

dx.doi.org/10.1021/ic500510s | Inorg. Chem. 2014, 53, 5280−5293

ratio is largest and the average Sc−Sc interaction strength is small relative to that of the Sc−Ir contacts. As either the Sc content of the coordination environment is increased (moving downward to lower y) or the average strength of the Sc−Sc interactions is enhanced (moving to the right toward higher x), the effect of the Ir neighbors on the ideal BF decreases. The degree of neutralization is then diminished, as is reflected in a lightening of the shading on the map.

Overlaid on this plot are positions calculated for the Sc-rich Sc−Ir phases discussed in this Article (black points), along with the several hypothetical structures with exclusively tcp or scp features (gray points; see Table 2 for a description of each structure). The experimentally observed and hypothetical crystal structures appear in different areas of the graph: the observed phases are clustered along a slightly slanted vertical line centered around $x \approx 0.55$, whereas the hypothetical structures all have x values of more than 1.1. As such, for any given composition, the experimental structures lie in a relatively darker region of the map, corresponding to better neutralization.

The stability trends for coordination environments with different Sc/Ir ratios are more difficult to evaluate. Just as with total energies, we cannot simply compare the RAs of two phases with different compositions. Instead we need to consider how the RA of a single phase compares with the average RA of a pair of neighboring phases in a ratio that gives the same Sc−Ir composition. This is done graphically in Figure 18, where pairs of experimentally observed Sc−Ir phases are connected by white curves corresponding to the (x, y) positions of the full range of linear combinations of the two phases at the ends. These white curves correspond to predicted stability ranges: a point to the right side of the curve lies in a lighter region of the map and will be susceptible to disproportionation into the two phases it connects. Meanwhile, a point to the left of the curve lies on its better-neutralized side and is predicted to be stable to disproportionation.

It is clear that all the observed phases are stable to disproportionation (no observed phase lies to the right of another white curve), whereas the hypothetical phases are highly unstable. If they could be prepared, then they would be predicted to convert spontaneously to a mixture of observed phases. ($Sc_{11}Ir_4$ sits right on the curve connecting Sc_2Ir and $Sc_{57}Ir_{13}$, indicating its critical position in the stability range.) The fact that the unobserved structures all lie to the right of these curves highlights that the $\overline{\mu_2^{A-A}}/\overline{\mu_2^{A-B}}$ parameter successfully resolves the hypothetical from the observed phases.

If we assume that the Sc−Ir interaction strength for each Sc−Ir contact is fixed at a constant favorable value across the Sc-rich Sc−Ir series, then $\overline{\mu_2^{A-A}}/\overline{\mu_2^{A-B}}$ can be readily interpreted in terms of the tcp and scp characteristics. This is illustrated in Figure 19 with a contour plot of the μ_2^{Sc-Sc} value as a function of d_{Sc-Sc} and σ_{Sc-Sc} (assuming a statistically normal distribution of Sc−Sc distances), upon which are overlaid the positions for the same series of structures as in Figure 18. Here, μ_2^{Sc-Sc} is minimized when the Sc−Sc distance distribution is narrow ($\sigma_{Sc-Sc} \approx 0$) and centered at a long distance. The μ_2^{Sc-Sc} increases when either (1) the average distance is decreased or (2) the width of the distribution increases (so that shorter distances are explored).

These two paths to increasing μ_2^{Sc-Sc} are followed by the pure scp or tcp structures, respectively. For scp structures, the Sc−Ir and Sc−Sc distances are essentially equal because of the regularity of the atomic positions. Relatively short Sc−Sc

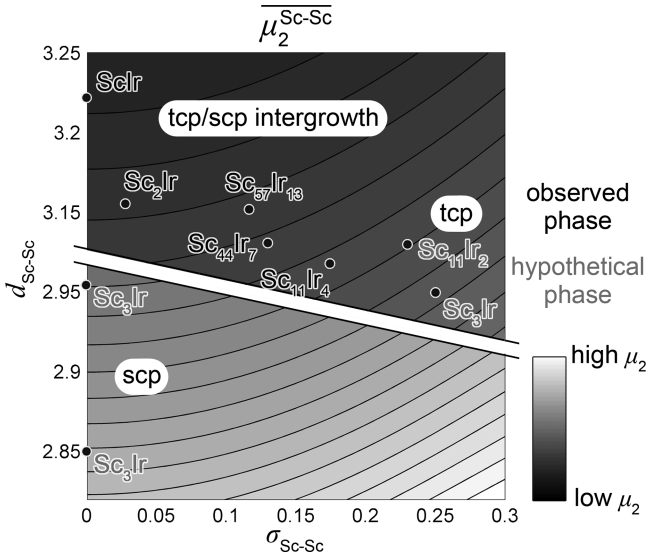

Figure 19. Contour plot of homoatomic μ_2 as a function of the mean and standard deviation of the Sc−Sc distance distribution. The observed phases achieved lower μ_2 values because of their longer Sc−Sc distances (compared to that of hypothetical scp phases) and more uniform Sc−Sc distance distribution (compared to that of hypothetical tcp phases). Note that part of the plot between d_{Sc-Sc} = 2.9 and 3.15 is omitted.

distances (2.95 or 2.85 Å vs sum of metallic radii = 3.24 Å) emerge from the need to accommodate Sc−Ir contacts (sum of metallic radii = 2.98 Å). In the tcp structures, the greater structural complexity allows for the Sc−Sc and Sc−Ir distances to be more independently varied. As such, the average Sc−Sc distances increase relative to those in the scp structures. However, the adoption of the tcp arrangement also introduced variations in the Sc−Sc distances, which increase μ_2^{Sc-Sc}.

In the observed tcp/scp intergrowth structures, both effects are largely avoided. The adoption of tcp arrangements immediately surrounding the Ir atoms allows for the Sc−Ir distances to be shorter than the Sc−Sc ones. Likewise, the arrangement of the Sc atoms onto scp substructures minimizes the variations among the Sc−Sc distances. As such, the observed tcp/scp intergrowth phases all lie in the upper left corner of the plot, where the μ_2^{Sc-Sc} values are the lowest. This placement, in turn, lowers their $\overline{\mu_2^{A-A}}/\overline{\mu_2^{A-B}}$ values and ultimately their residual acidities.

In this section, we have supplemented with a quantitative analysis our structural survey of the tcp/scp features of the Sc-rich Sc−Ir phases favorable for μ_3 neutralization. Using the functions connecting μ_3 neutralization to the features of a crystal structure, we have seen that the stability trends across this family of compounds can be simply understood in terms of a handful of basic parameters: the ratio of Sc and Ir neighbors in the coordination environments of the majority Sc atoms, the mean Sc−Sc distance, and the standard deviation of the Sc−Sc distances. The incorporation of both scp and tcp features into the observed crystal structures allows for the distributions of interatomic distances to maximize the neutralization possible for a given Sc/Ir ratio.

10. CONCLUSIONS

In this Article, we have used the μ_3-acidity model to account for the structural diversity across the Sc-rich phases of the Sc−Ir system. The challenges faced by these structures were

dx.doi.org/10.1021/ic500510s | Inorg. Chem. 2014, 53, 5280−5293

anticipated by our results for the CsCl-type ScIr phase, which indicated that the acid−base strengths of the two elements are well-matched at a 1:1 stoichiometry. Moving to more Sc-rich compositions is then expected to lead to the majority Sc atoms needing to achieve neutrality with a smaller number of Ir neighbors. Under these conditions, the structures maximize the neutralizing effect of Sc−Ir interactions by adopting intergrowths of tetrahedral and simple close-packed (tcp and scp) arrangements: the construction of tcp arrangements around the Ir atoms enhances the interaction strength between the Sc and Ir atoms, whereas the organization of the Sc atoms into scp frameworks serves to dampen the role of Sc−Sc interactions.

Through the incorporation of these tcp/scp intergrowth features, all of the observed Sc-rich Sc−Ir phases exhibit lower Sc residual acidities than combinations of neighboring phases of the same net composition. In this way, the μ_3-acidity model not only reveals stabilizing features within the individual crystal structures but also recovers the stabilities of the phases relative to disproportation into more Sc-rich and Sc-poor phases.

The success of this simple model in predicting the form of the phase diagram probably stems from the high acidity and basicity of Sc and Ir, respectively, which could make μ_3 neutralization a large factor governing the energies of the phases. It will be interesting to examine how well such considerations can be used to rationalize the phases observed in binary systems with weaker μ_3-acids and -bases. One trend that we anticipate will recur is that μ_3 neutralization is not a simple function of stoichiometry but has a strong dependence on structural features: the stoichiometry of an observed compound reflects the ability of its crystal structure to provide higher neutralization than competing combinations of phases.

The emerging picture of structural acid−base chemistry presented here also has implications for the ways structural incompatibilities may arise in intermetallic phases. tcp and scp arrangements represent distinct forms of atomic packing, which would seem more likely to phase segregate than aggregate together in the same crystal structures. The μ_3-acidity model provides one approach for encouraging their intergrowth: combine a strong μ_3-acid with a strong μ_3-base in grossly uneven ratios. The majority element will be expected to adopt scp features with itself while enclosing the atoms of the minority element in tcp polyhedra.

Such features are frequently observed in compounds formed between a majority electropositive metal and a minority electronegative metal. As in the recent examples Ca_5Cu_2Cd and $Ca_2Cu_2Cd_9$,[49] the electropositive metals of the scp components often come from the alkaline earth, lanthanide, or group 12 series. Accounting for this family as a whole will thus require adapting the μ_3-acidity model beyond d-block metals. Our group is currently finalizing such a generalized μ_3-acidity method in which Wannier-type functions[50,51] are used to extract the essential interactions to be included in the calculations of the moments.

In the Sc−Ir system, one product of tcp/scp intergrowth is the icosahedral cluster prominent in Mackay-type quasicrystals and their approximants. These emerge as Sc−Ir tcp icosahedra serve the nuclei for a Sc−Sc scp domain. The resulting core−shell segregation between Sc−Ir and Sc−Sc interactions mirrors a similar micelle-like separation of Ca−Cd and Cu−Cd interactions in the Bergman-type clusters of $Ca_{10}Cd_{27}Cu_2$.[52] Such parallels between the origins of local icosahedral order for two different families of quasicrystals (Mackay- and Bergman-type) hint at a more general role for the chemical frustration between interaction types in quasicrystalline order.

■ ASSOCIATED CONTENT

Ⓢ Supporting Information

Detailed theoretical procedures; optimized coordinates and total energies for Sc−Ir phases; description of the best-fit curve in Figure 5; plot of the average residual acidities taken over all atoms as a function of Ir/Sc ratio; DFT-calibrated Hückel parameters; and μ_3-acidity results for the Sc−Ir phases. This material is available free of charge via the Internet at http://pubs.acs.org.

■ AUTHOR INFORMATION

Corresponding Author

*E-mail: danny@chem.wisc.edu.

Present Address

†(T.E.S.) Department of Chemistry and Biochemistry, and Department of Physics, University of Maryland, College Park, Maryland 20742, United States.

Notes

The authors declare no competing financial interest.

■ ACKNOWLEDGMENTS

We gratefully acknowledge the financial support of the U.S. DOE Office of Science Early Career Program (DE-SC0003947) through the Office of Basic Energy Sciences. This research involved calculations using computer resources supported by National Science Foundation grant CHE-0840494.

■ REFERENCES

(1) Pearson, W. B. *The Crystal Chemistry and Physics of Metals and Alloys*; Wiley-Interscience: New York, 1972.

(2) Daams, J. L. C.; Villars, P.; van Vucht, J. H.; Miedema, A. R. *Atlas of Crystal Structure Types for Intermetallic Phases*; ASM International: Materials Park, OH, 1991.

(3) Villars, P.; Calvert, L. D. *Pearson's Handbook of Crystallographic Data for Intermetallic Phases*, 2nd ed.; ASM International: Materials Park, OH, 1991.

(4) Zintl, E. *Angew. Chem.* **1939**, *52*, 1−6.

(5) Schäfer, H.; Eisenmann, B.; Müller, W. *Angew. Chem., Int. Ed. Engl.* **1973**, *12*, 694−712.

(6) *Chemistry, Structure, And Bonding of Zintl Phases and Ions*; Kauzlarich, S. M., Ed.; VCH: New York, 1996.

(7) Corbett, J. D. *Inorg. Chem.* **2009**, *49*, 13−28.

(8) Wang, F.; Miller, G. J. *Inorg. Chem.* **2011**, *50*, 7625−7636.

(9) Wang, F.; Miller, G. J. *Eur. J. Inorg. Chem.* **2011**, 3989−3998.

(10) Brewer, L.; Wengert, P. *Metall. Trans.* **1973**, *4*, 83−104.

(11) Stacey, T. E.; Fredrickson, D. C. *Inorg. Chem.* **2012**, *51*, 4250−4264.

(12) Stacey, T. E.; Fredrickson, D. C. *Dalton Trans.* **2012**, *41*, 7801−7813.

(13) Stacey, T. E.; Fredrickson, D. C. *Inorg. Chem.* **2013**, *52*, 8349−8359.

(14) Yeremenko, V. N.; Khorujaya, V. G.; Martsenyuk, P. S. *J. Alloys Compd.* **1994**, *204*, 83−87.

(15) Okamoto, H. *J. Phase Equilib.* **1997**, *18*, 224−225.

(16) Chabot, B.; Cenzual, K.; Parthé, E. *Acta Crystallogr., Sect. B* **1980**, *36*, 7−11.

(17) Mackay, A. *Acta Crystallogr.* **1962**, *15*, 916−918.

(18) Steurer, W.; Deloudi, S. *Acta Crystallogr., Sect. A* **2008**, *64*, 1−11.

(19) Cenzual, K.; Chabot, B.; Parthé, E. *Acta Crystallogr., Sect. C* **1985**, *41*, 313−319.

(20) Chabot, B.; Cenzual, K.; Parthé, E. *Acta Crystallogr., Sect. B* **1980**, *36*, 2202−2205.

(21) Mizutani, U.; Kondo, Y.; Nishino, Y.; Inukai, M.; Feuerbacher, M.; Sato, H. *J. Phys.: Condens. Matter* **2010**, *22*, 485501.
(22) Bergerhoff, G.; Hundt, R.; Sievers, R.; Brown, I. D. *J. Chem. Inf. Comput. Sci.* **1983**, *23*, 66−69.
(23) Bergerhoff, G.; Brown, I. D. In *Crystallographic Databases*; Allen, F. H., Bergerhoff, Sievers, R., Eds.; International Union of Crystallography: Chester, England, 1987.
(24) Belsky, A.; Hellenbrandt, M.; Karen, V. L.; Luksch, P. *Acta Crystallogr., Sect. B* **2002**, *58*, 364−369.
(25) Kresse, G.; Furthmüller, J. *Comput. Mater. Sci.* **1996**, *6*, 15−50.
(26) Kresse, G.; Furthmüller, J. *Phys. Rev. B* **1996**, *54*, 11169−11186.
(27) Blöchl, P. E. *Phys. Rev. B* **1994**, *50*, 17953−17979.
(28) Kresse, G.; Joubert, D. *Phys. Rev. B* **1999**, *59*, 1758−1775.
(29) Landrum, G. A.; Glassey, W. V. YAeHMOP: Yet Another Extended Hückel Molecular Orbital Package, Ver. 3.0. YAeHMOP is freely available at http://yaehmop.sourceforge.net/.
(30) Cyrot-Lackmann, F. *J. Phys., Colloq.* **1974**, 109−114.
(31) Burdett, J. K.; Lee, S. *J. Am. Chem. Soc.* **1985**, *107*, 3050−3063.
(32) Lee, S. *Annu. Rev. Phys. Chem.* **1996**, *47*, 397−419.
(33) Clark, P. M.; Lee, S.; Fredrickson, D. C. *J. Solid State Chem.* **2005**, *178*, 1269−1283.
(34) Pettifor, D. G.; Oleynik, I. I. *Prog. Mater. Sci.* **2004**, *49*, 285−312.
(35) Aste, T.; Weaire, D. L. *The Pursuit of Perfect Packing*; Institute of Physics Pub.: Philadelphia, PA, 2000.
(36) Frank, F. C.; Kasper, J. S. *Acta Crystallogr.* **1958**, *11*, 184−190.
(37) Frank, F. C.; Kasper, J. S. *Acta Crystallogr.* **1959**, *12*, 483−499.
(38) Oberteuffer, J. A.; Ibers, J. A. *Acta Crystallogr., Sect. B* **1970**, *26*, 1499−1504.
(39) Uchishiba, H. *J. Phys. Soc. Jpn.* **1971**, *31*, 436−440.
(40) Kotur, B. Y.; Bodak, O. I.; Andrusyak, R. I.; Zavodnik, V. E.; Bel'skii, V. K. *Dopov. Akad. Nauk Ukr. RSR, Ser. B: Geol., Khim. Biol. Nauki* **1986**, 28−31.
(41) Kim, W. J.; Gibbons, P. C.; Kelton, K. F. *Philos. Mag. A* **1998**, *78*, 1111−1124.
(42) Kim, W. J.; Gibbons, P. C.; Kelton, K. F.; Yelon, W. B. *Phys. Rev. B* **1998**, *58*, 2578−2585.
(43) Westin, L.; Edshammar, L. E. *Acta Chem. Scand.* **1972**, *26*, 3619−3626.
(44) Berger, R. F.; Lee, S.; Hoffmann, R. *Chem.—Eur. J.* **2007**, *13*, 7852−7863.
(45) Berger, R. F.; Lee, S.; Johnson, J.; Nebgen, B.; Sha, F.; Xu, J. *Chem.—Eur. J.* **2008**, *14*, 3908−3930.
(46) Ilyushin, G. D.; Blatov, V. A. *Russ. J. Inorg. Chem.* **2010**, *55*, 1909−1918.
(47) Keggin, J. F. *Proc. R. Soc. London, Ser. A* **1934**, *144*, 75−100.
(48) Pang, Q.; Zhao, L.; Cai, Y.; Nguyen, D. P.; Regnault, N.; Wang, N.; Yang, S.; Ge, W.; Ferreira, R.; Bastard, G.; Wang, J. *Chem. Mater.* **2005**, *17*, 5263−5267.
(49) Harris, N. A.; Hadler, A. B.; Fredrickson, D. C. *Z. Anorg. Allg. Chem.* **2011**, *637*, 1961−1974.
(50) Wannier, G. H. *Phys. Rev.* **1937**, *52*, 191−197.
(51) Marzari, N.; Mostofi, A. A.; Yates, J. R.; Souza, I.; Vanderbilt, D. *Rev. Mod. Phys.* **2012**, *84*, 1419−1475.
(52) Hadler, A. B.; Harris, N. A.; Fredrickson, D. C. *J. Am. Chem. Soc.* **2013**, *135*, 17369−17378.